

# Cosmography with cluster strong lensing

James Gilmore<sup>1\*</sup> and Priyamvada Natarajan<sup>1,2,3†</sup>

<sup>1</sup>*Department of Physics, Yale University, P.O. Box 208120, New Haven, CT 06520-8120, USA*

<sup>2</sup>*Department of Astronomy, Yale University, P.O. Box 208101, New Haven, CT 06520-8101, USA*

<sup>3</sup>*Radcliffe Institute for Advanced Study, 10 Garden Street, Cambridge, MA 02138*

7 July 2018

## ABSTRACT

By stacking an ensemble of strong lensing clusters, we demonstrate the feasibility of placing constraints on the dark energy equation of state. This is achieved by using multiple images of sources at two or more distinct redshift planes. The sample of smooth clusters in our simulations is based on observations of massive clusters and the distribution of background galaxies is constructed using the Hubble Deep Field. Our source distribution reproduces the observed redshift distribution of multiply imaged sources in Abell 1689. The cosmology recovery depends on the number of image families with known spectroscopic redshifts and the number of stacked clusters. Our simulations suggest that constraints comparable to those derived from other competing established techniques on a constant dark energy equation of state can be obtained using 10 to 40 clusters with 5 or more families of multiple images. We have also studied the observational errors in the image redshifts and positions. We find that spectroscopic redshifts and high resolution *Hubble Space Telescope* images are required to eliminate confidence contour relaxation relative to the ideal case in our simulations. This suggests that the dark energy equation of state, and other cosmological parameters, can be constrained with existing *Hubble Space Telescope* images of lensing clusters coupled with dedicated ground-based arc spectroscopy.

**Key words:** cosmological parameters — gravitational lensing — clusters

## 1 INTRODUCTION

Current efforts in observational cosmology are directed towards characterizing the energy content of the Universe. The discovery of the accelerating expansion of the Universe inferred from the Hubble diagram for SN type Ia (Riess et al. 1998; Perlmutter et al. 1999; Tonry et al. 2003; Riess et al. 2004, 2007) combined with constraints from Cosmic Microwave Background Radiation from the Wilkinson Microwave Anisotropy Probe (Spergel et al. 2003, 2007; Hinshaw et al. 2009), from cosmic shear observations (Bacon, Refregier & Ellis 2000; Kaiser 2000; van Waerbeke et al. 2000; Wittman et al. 2000; Semboloni et al. 2006), cluster baryon fractions (Allen et al. 2004), galaxy surveys (Efstathiou et al. 2002; Seljak et al. 2005) suggests that  $\sim 70$  per cent of the energy in the Universe is in the form of dark energy. Dark energy is best described by the equation of state that relates its pressure,  $P$ , to its energy density,  $\rho$ , via  $P = w_x \rho$ , with  $w_x = -1$  corresponding to the case of the cosmological constant.

Massive foreground clusters often produce many sets

of highly distorted arcs and multiple images of background galaxies (Blandford & Narayan 1992). The lensing effect is determined by the mass distribution, the precise configuration of the lens and source with respect to the observer, and the angular diameter distances between the lens, source and observer. When at least two sources at distinct redshift are strongly lensed in a cluster, the relative positions of the arcs depend on the ratios of angular diameter distances. In principle therefore, cosmological parameters can be constrained from the lensing configuration.

Constraining the geometry and matter content of the Universe using multiple sets of arcs in cluster lenses has been explored by Paczynski & Gorski (1981); Link & Pierce (1998); Cooray (1999); Golse, Kneib, & Soucail (2002); Sereno (2002); Soucail, Kneib & Golse (2004). Recently, Biesiada (2006) has suggested using multiple images produced by galaxy lenses instead of clusters and attempted an application to the case of the lensing system HST14176+5226. Link & Pierce (1998) showed that the cosmological sensitivity of the angular size-redshift relation could be exploited using sources at distinct redshifts and developed a methodology to simultaneously invert the lens and derive cosmological constraints. Sereno (2002) applied the technique to the cluster Cl0024+1654 and found sup-

\* E-mail: james.gilmore@yale.edu

† E-mail: priya@astro.yale.edu

port for an accelerating Universe. Golse, Kneib, & Soucail (2002) showed that the recovery of cosmological parameters was feasible with 3 sets of multiple images for a single simulated cluster. Soucail, Kneib & Golse (2004) then applied the technique to the lensing cluster Abell 2218 and using 4 multiple image systems at distinct redshifts, find  $\Omega_M < 0.37$  and  $w < -0.80$  assuming a flat Universe. Recently, a double Einstein ring has been discovered and applied to cosmography (Gavazzi et al. 2008). As the system has only two sources, only weak cosmography constraints were obtained.

There have been several studies that have explored the cross-sections of multiple image formation using simulated clusters from cosmological  $N$ -body simulations. Meneghetti et al. (2005a,b) and Macciò (2005) studied the efficiency of numerical clusters to produce multiple images in different dark energy models. They found the expected abundance of arcs with a given length-to-width ratio and the lensing cross-sections depend on the equation of state of dark energy. These statistical studies of multiple image formation concluded that strong lensing offers a plausible method to discriminate amongst various dark energy models.

In this paper we study two basic aspects of the non-statistical approach to cosmography with cluster strong lensing (CSL), which have yet to be addressed. These are: 1) How many clusters must be individually marginalized, with the resulting  $\chi^2$  from each cluster added together to form a final  $\chi^2$  for cosmology recovery (i.e. stacked), in the ideal case to obtain cosmological constraints comparable with other methods and 2) The required accuracy of the observational parameters, i.e. the source redshift and image positions. By studying these two aspects separately from the subtleties involved with cluster mass distribution reconstruction, we can make definitive statements on the type of cluster surveys required for a first application of CSL.

We do not model the lensing effects induced by the distribution of substructure along the line of sight. This additional complication has been examined in earlier work by Wambsganss, Bode & Ostriker (2005) and Dalal, Hennawi & Bode (2005), who both used ray tracing methods through  $N$ -body simulations. Simulating a representative shell of the Universe centered at  $z = 1$ , Wambsganss, Bode & Ostriker (2005) found that approximately 10%-15% of the lensing mass was to be found in substructure along the line of sight, for about one third of lensing configurations with a source redshift above  $z_s = 2.5$ . In particular, it was shown that substructure along the line of sight is limited to a finite number of lens planes, typically one or two additional planes, when line of sight substructure played a significant role in lensing. They have shown explicitly that  $< 20\%$  of the contribution to the convergence arises from secondary lens planes. For cluster strong lensing the critical factor is not the error induced in the convergence but rather the perturbations caused in the positions of the multiple images due to the presence of matter in additional lens planes. A detailed and exhaustive set of cosmological simulations that will enable the matter distribution of a typical line of sight to be averaged over many representative lines of sight is needed to accurately quantify this effect. In Dalal, Hennawi & Bode (2005) it was shown that systematic errors in the cosmology recovery could result, if the line of sight substructure was not taken into account.

The outline of this paper is as follows: we begin with an introduction to the basics of strong lensing and dark energy in Section 2. Then in Section 3 we discuss image families, and define the cosmological family ratio, which CSL constrains. The methodology used to generate smooth simulated clusters is described in Section 4 and Section 5, along with the  $\chi^2$  minimization scheme used in the cosmology recovery. We present the results of recovering the input cosmology in Section 6, and study the dependence of the recovery on lens parameters in Section 7. We then study the allowed errors in the source redshift and image positions in Section 8. This is followed by a discussion of the simplifying assumptions made in this work in Section 9. We conclude with a summary of our technique, and the implications for future survey strategies.

## 2 STRONG GRAVITATIONAL LENSING AND DARK ENERGY

The gravitational lens equation is a mapping from the source plane at redshift  $z_s$  to the image plane (or lens plane) at redshift  $z_l$  and is given by,

$$\boldsymbol{\theta} = \boldsymbol{\beta} + \boldsymbol{\alpha}(\boldsymbol{\theta}, \xi; M) \quad (1)$$

where  $\boldsymbol{\theta}$  is the angular position of the image,  $\boldsymbol{\beta}$  is the unobserved source position,  $\boldsymbol{\alpha}$  is the deflection angle which depends on  $\xi$  the reduced angular diameter distance,  $M$  the mass distribution of the lens and  $\boldsymbol{\theta}$ . The cosmological dependence is contained in  $\xi$ , which we call the reduced angular diameter defined by:  $\xi = D(0, z_l)D(z_l, z_s)/D(0, z_s) \equiv D_{ol}D_{ls}/D_{os}$ , where  $D(z_1, z_2)$  is the angular diameter distance between redshift  $z_1$  and  $z_2$ , and  $D_{ol}$ ,  $D_{ls}$  and  $D_{os}$  are the observer-lens, lens-source and observer-source angular diameter distances respectively. In a flat homogeneous Friedmann-Robertson-Walker cosmology the angular diameter distance is given by,

$$D(z_1, z_2) = \frac{cH_0^{-1}}{1+z_2} \int_{z_1}^{z_2} dz \left( \Omega_M(1+z)^3 + \Omega_X(1+z)^{3(w_X+1)} \right)^{-1/2} \quad (2)$$

where  $c$  is the speed of light;  $H_0 = 100 h \text{ km s}^{-1}$  is the present day value of the Hubble constant, and  $\Omega_M$  and  $\Omega_X$  are the fractional contributions of the total matter and dark energy respectively, in units of the critical density and  $w_X$  is the dark energy equation of state. Note that we do not consider evolving dark energy models in our simulations, since there is currently no observational evidence for such a time evolution in the dark energy equation of state (Sahni & Starobinsky 2006; Komatsu et al. 2009).

To further explore the dependence of the lens equation on cosmological parameters, we note that the deflection angle can be written in terms of the gradient of the reduced gravitational potential  $\varphi_M(\boldsymbol{\theta}, \xi)$ :  $\nabla \varphi_M(\boldsymbol{\theta}, \xi) = \boldsymbol{\alpha}(\boldsymbol{\theta}, \xi; M)$ . The reduced gravitational potential can be related to the projected surface mass density along the line of sight,  $\Sigma_M(\boldsymbol{\theta})$ , through the Poisson equation, where the projected gravitational potential  $\phi_M(\boldsymbol{\theta})$  is defined by

$$\varphi_M(\boldsymbol{\theta}, \xi) = \xi \frac{2}{c^2} \phi_M(\boldsymbol{\theta}). \quad (3)$$

In the thin lens approximation the projected gravitational potential is a solution of:  $\nabla^2 \varphi_M(\boldsymbol{\theta}, \xi) = 8\pi G \xi \Sigma_M(\boldsymbol{\theta})/c^2$ .

The total deflection ( $\theta - \beta$ ) is therefore determined both by the cosmological parameters (via  $D_{\text{ol}}D_{\text{ls}}/D_{\text{os}}$ ) and the projected surface mass density of the intervening lens. For a given configuration of the source, lens and observer, the critical value of the surface mass density is:

$$\Sigma_{\text{crit}} = \frac{c^2}{4\pi G} \frac{1}{\xi}. \quad (4)$$

The region where the projected surface mass density of a lens exceeds this critical value defines the strong lensing regime. Background sources that are aligned behind this region are likely to be multiply imaged, magnified and distorted.

There are hence two fundamental equations which define the gravitational lensing dependence on the angular diameter distances  $D_{\text{ol}}, D_{\text{ls}}, D_{\text{os}}$ . The first is the lens mapping, equation (1), which defines the configuration of the images produced by a lensing cluster, and the second is equation (4) which defines the strong lensing regime. The cosmological dependence of strong lensing is discussed further in Section 3.

### 3 THE COSMOLOGICAL FAMILY RATIO

#### 3.1 Multiple image families

Consider a lensing configuration where at least two sources have been strongly lensed by a cluster. Once the multiple images of each source have been identified, we can write the source and the associated image positions with a family index  $f$ . The lens equation is then,

$$\beta_f = \theta_{f,i} - \nabla\phi_M(\theta_{f,i}, \xi), \quad (5)$$

where  $\theta_{f,i}$  denotes the position of the  $i^{\text{th}}$  image of family  $f$ . When there are  $k$  multiple images detected in family  $f$ , we can sum over all the images in equation (5). Substituting into equation (3) for the reduced gravitational potential allows the summed equation to be written in terms of the line of sight projected gravitational potential as follows:

$$\sum_{i=1}^k \theta_{f,i} = \frac{2}{c^2} \left( \frac{D_{\text{ls}}}{D_{\text{ol}}D_{\text{os}}} \right) \sum_{i=1}^k \nabla\phi_M(\theta_{f,i}) + k\beta_f. \quad (6)$$

Note that equation (6) is a non-linear function of the image positions, since the sum of the image positions depends on the projected cluster potential gradient.

Given a set of input cosmological parameters, the lens redshift and a source redshift for a single family of images, i.e.  $(z_l, z_s, \Omega_M, \Omega_X, w_X)$ , the angular diameter distance ratio is specified and constant. The cluster potential is conventionally normalized by the square of the velocity dispersion, which we denote by  $v$ . In equation (6) the reduced angular diameter distance  $\xi$  and the cluster mass normalization  $v^2$  are degenerate when recovering cosmological parameters. *Therefore, cosmological parameters cannot be disentangled from the cluster mass normalization with only one family of multiple images.* Possible solutions to remove this degeneracy are considered by Golse, Kneib, & Soucail (2002). They show an additional prior on the mass profile is required and this must come from observations independent of strong lensing. For parametric models, this is typically a total mass determination from the detected X-ray emission of the cluster.

#### 3.2 Two families of multiple images

Now consider the case when two strongly lensed sources are observed as multiple image families in the same cluster lens at two redshifts. Let family 1 have a total of  $m$  observed images and family 2 have  $n$  observed images. We require that at least two images from each are observed, i.e.  $m, n \geq 2$ . Taking the ratio of family 1 to family 2 (equation [6]) we obtain,

$$\left\{ \frac{D_{\text{ls1}} D_{\text{os2}}}{D_{\text{os1}} D_{\text{ls2}}} \right\} \frac{\sum_{i=1}^m \nabla\phi_M(\theta_{1,i})}{\sum_{j=1}^n \nabla\phi_M(\theta_{2,j})} = \frac{-m\beta_1 + \sum_{i=1}^m \theta_{1,i}}{-n\beta_2 + \sum_{j=1}^n \theta_{2,j}}. \quad (7)$$

Note that we now have a ratio of two factors of  $\nabla\phi_M(\theta)$ . This clearly means that the degeneracy between the cosmological parameters and the cluster potential normalization is broken when 2 families of multiple images are observed in a cluster lens.

In equation (7), the term in braces is a function of the angular diameter distances only. This quantity is fundamental to the determination of cosmological parameters through CSL and we define this term as the family ratio and denote it by  $\Xi$ :

$$\Xi(z_l, z_{s1}, z_{s2}; \Omega_M, \Omega_X, w_X) = \frac{D(z_l, z_{s1}) D(0, z_{s2})}{D(0, z_{s1}) D(z_l, z_{s2})} \quad (8)$$

where  $z_l$  is the lens redshift,  $z_{s1}$  and  $z_{s2}$  are the two source redshifts, and  $D(z_1, z_2)$  is the angular diameter distance defined in equation (2). The cosmological family ratio can be written in terms of the reduced angular diameter distance,  $\Xi = \xi_1/\xi_2$ , where the subscripts 1 and 2 here denote the family index.

We plot  $\Xi$  in Fig. 1 for a fixed lens redshift of  $z_l = 0.3$  and differing source redshifts. Since the non-evolving dark energy component with  $w_X = -1$  can also be interpreted as the cosmological constant  $\Omega_\Lambda$ , we plot the contours of the cosmological family ratio in both the  $\Omega_M$ - $\Omega_\Lambda$  plane in addition to the  $\Omega_M$ - $w_X$  plane. Note that the contours in the  $\Omega_M$ - $\Omega_\Lambda$  plane are not as sensitive to the lens-source configuration as they are in the  $\Omega_M$ - $w_X$  plane.

### 4 SIMULATIONS OF STRONG LENSING CLUSTERS

As shown in the previous section, the cosmological family ratio,  $\Xi$ , depends on the source redshifts and the lens redshift (see Fig. 1). It is therefore clear that the distribution of sources in magnitude and redshift as well as the cluster redshift distribution are key inputs in our simulations. Therefore we base our simulations of strong lensing clusters on high resolution observational data from *HST* images. We note that although the cluster normalization is irrelevant to our method for constraining the cosmological parameters, we still construct this quantity rigorously. This ensures the simulations produce lensing clusters with cross-sections similar to those of observed clusters.

#### 4.1 Source magnitude and redshift distribution

In order to simulate the lensed images produced by a massive cluster, it is necessary to characterize the number density,  $N$ , of the sources behind the lens. We consider back-

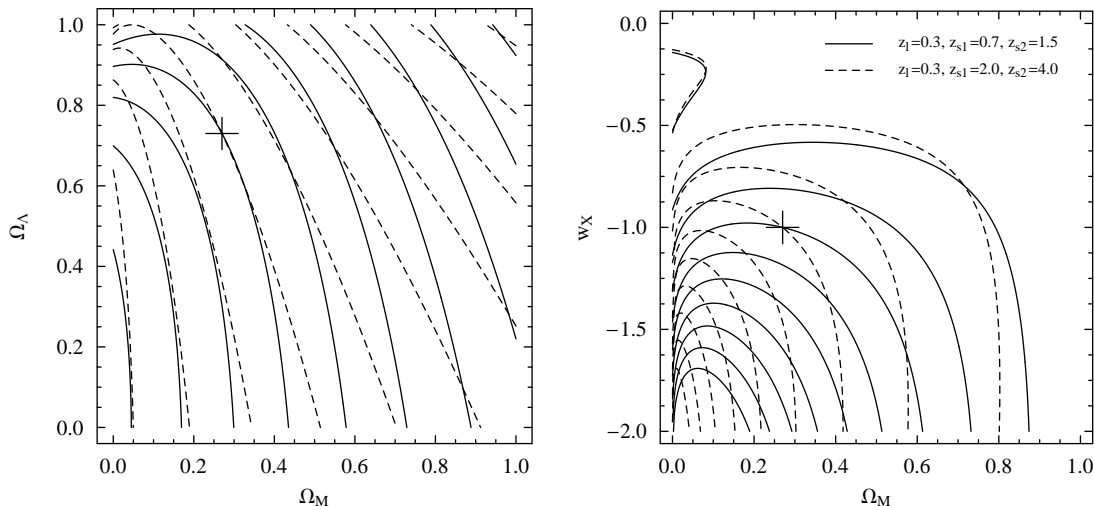


**Figure 1.** Contours of the cosmological family ratio  $\Xi(z_1, z_{s1}, z_{s2}; \Omega_M, \Omega_X, w_X)$  on the  $\Omega_M$ - $\Omega_\Lambda$  and  $\Omega_M$ - $w_X$  planes. The cross marks the input cosmology. The redshift of the lensing cluster is fixed at  $z_1 = 0.3$ . Solid contours correspond to sources at  $z_{s1} = 0.7$ ,  $z_{s2} = 1.5$  and dashed to sources at  $z_{s1} = 2.0$ ,  $z_{s2} = 4.0$  in both panels.

ground point sources for which the number density is a function of magnitude and redshift, i.e.  $N = N(m, z)$ . Furthermore, space-based positional accuracy is assumed throughout this paper. We must therefore draw redshifts and magnitudes from a space-based source distribution. The Hubble Deep Field (HDF) Williams et al. (1996) and HDF-South (HDF-S) WFPC2 Casertano et al. (2000) are the ideal data sets to derive the source distribution. It is also possible to use the recent COSMOS data to derive the redshift and magnitude source distributions, see Gabasch et al. (2008). In particular we have checked that our source redshift distribution, which is derived below, is equivalent to that of Gabasch et al. (2008).

We employ the WFPC2 HDF and HDF-S photometric redshift catalogues derived by the Stony Brook collaboration (Fernández-Soto, Lanzetta, & Yahil 1999; Yahata et al. 2000) and characterize the HDF sources by a distribution function. This method is chosen since we wish to analyse an ensemble of clusters, where each cluster lenses a unique source configuration. Characterizing the source distribution by a function is preferable in our case, since we do not want to bias the results by lensing large scale structures such as voids or filaments. Note that there is evidence of a weak cluster in the HDF (Villumsen, Freudling & da Costa 1997).

To model the source distribution from the HDF and HDF-S data, we first make two cuts to the catalogues. Initially, we drop all objects with magnitudes greater than  $AB(8140) = 28.00$ . Next we select objects in the redshift interval  $0.4 \leq z \leq 5.0$ . The lower bound is chosen because the lensing efficiency is negligible for low source redshifts. The upper redshift bound is chosen because the photometric redshift determination is unreliable for  $z \gtrsim 5.0$  and most observed multiply imaged sources behind massive clusters have redshift  $z \lesssim 5.0$ . This yields 1688 objects when the catalogues are merged. The corresponding projected source number density is  $215 \text{ arcmin}^{-2}$  for the ensemble catalogue.

We now bin the merged catalogue in magnitude from

$AB(8140) = 19.0 - 28.0$  in intervals of 0.5 and in redshift from  $z = 0.4 - 5.0$  in intervals of 0.2. These data are then fit with functions of the form,

$$N(m, z) = f \exp[-a(m-b)^s] \exp[-c(z-d)^t] \times \exp[-g(m-b)^u(z-d)^v], \quad (9)$$

where the exponents in the exponential terms,  $(s, t, u, v)$ , can take an even integer value. The constants  $a, b, c, d$ , and  $f$  are determined in the fitting procedure. We simply use the lowest  $\chi^2$  fit to construct a probability distribution function in the simulations. This is  $(s, t, u, v) = (4, 2, 8, 2)$ , with the other parameters given by:  $a = 1.607 \times 10^{-4}$ ,  $b = 30.70$ ,  $c = 9.97 \times 10^{-2}$ ,  $d = 0.507$ ,  $g = 2.197 \times 10^{-7}$  and  $f = 18.462$ .

Notably, the  $\chi^2$  of the above fit is approximately one half of the  $\chi^2$  that is obtained when the binned magnitude and redshift data are decoupled and fitted on an individual basis, i.e.  $N(z)$  and  $N(m)$ . It is therefore clear that to avoid a systematic bias in the source generation, a joint fit in magnitude and redshift space is required.

#### 4.1.1 Comparison to Abell 1689

Deep ACS imaging of Abell 1689 has allowed identification of more than 30 families of multiply images systems (Broadhurst et al. 2005; Limousin et al. 2007). It is clear that Abell 1689 is the ideal candidate to compare with our source distribution. We base our analysis on Broadhurst et al. (2005), however our conclusions are unchanged if we use the analysis of Limousin et al. (2007). With the lens model as a guide Broadhurst et al. (2005) have identified multiple images to  $I = 29.82$ . This means images with magnitudes comparable to and less than the magnitude limit of our HDF catalogues,  $AB(8140) = 28.00$ , are detected in the ACS observations. This means we can compare our source distribution to the properties of Abell 1689 directly.

In order to compare the source characteristics of Abell

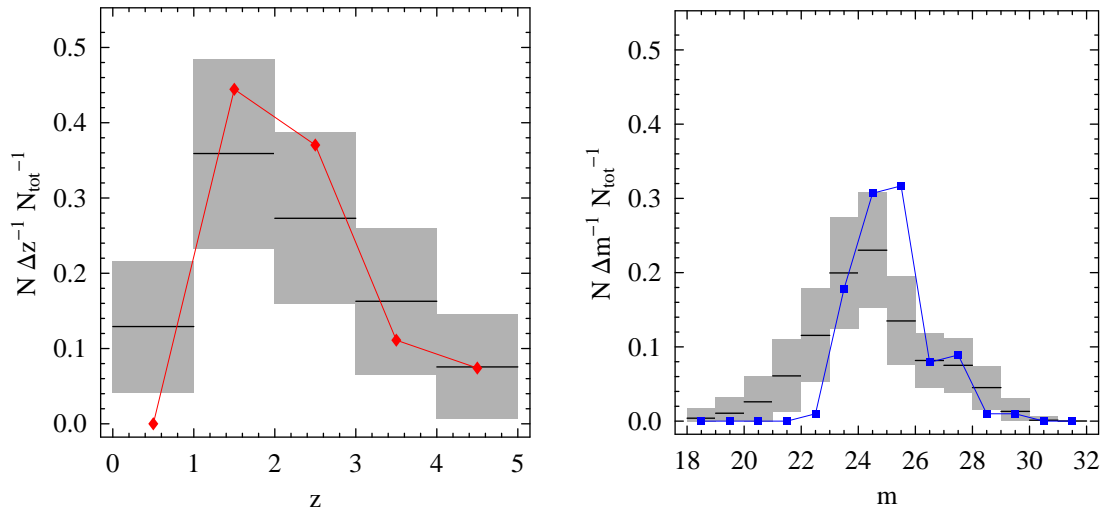


**Figure 2.** Comparison of image properties using the lensed HDF derived distribution and the Abell 1689 data of Broadhurst et al. (2005). In each bin, the simulated data has a mean given by the solid horizontal line and the gray rectangle represent  $\pm 1\sigma$ . *Left panel:* Redshift distributions. The Abell 1689 data are plotted as solid diamonds. *Right panel:* Magnitude distributions. The solid squares are the Abell 1689 data.

1689 with our source distribution, we need to lens this distribution through a mass model. Broadhurst et al. (2005) have published an Navarro, Frenk, & White (NFW) fit (see Section 4.3.1) to approximate the true mass profile. Using a radially averaged (and therefore circular) mass profile, they provide the tangential and radial critical curves, computed at redshift  $z = 3.0$ . They also determine the NFW scale radius  $r_s = 473_{-169}^{+197}$  kpc and we adopt  $r_s = 473$  kpc. We then adjust an NFW fit until the two critical curve locations are reproduced.

Since we are using a smooth profile, the properties of Abell 1689 we compare our source distribution with cannot depend on the small scale details of the mass distribution. There are two quantities which satisfy this requirement: 1) the total number of lensed sources and 2) their redshift distribution. A test of the HDF constructed source distribution would be the ability to reproduce these two quantities for simulated lenses similar to Abell 1689. Note that we do expect some systematic effects due to the lack of assumed substructure in the modeling. In particular, the fact that Abell 1689 is non-circular, and is known to have images which are influenced by substructure, means any comparison between the actual data and our model (which is circular, and has no structure) will exhibit residuals.

To compare our simulations with the Abell 1689 sources, we take  $z_{\text{best}}$  as the source redshift for each image from table 2 of Broadhurst et al. (2005). Also, because the HDF catalogues used to derive the source distribution have been cut at  $z = 5.0$ , we drop all sources with redshift  $z > 5.0$ . The Abell 1689 source redshifts are then binned in intervals of  $\Delta z = 1.0$  from  $z = 0.0$  to  $z = 5.0$ . For proper comparison with the simulations, the bin counts are normalized by the total number of families in Abell 1689.

We simulate the smooth Abell 1689 NFW profile for 500 source configurations generated with our source distribution. We then lens the sources independently for each configuration, using the procedure explained in Section 5.1. Multiply

imaged sources are identified and binned identically as the Abell 1689 sources.

The average number of multiply imaged sources in the 500 simulations is  $N_{\text{sim}} = 16 \pm 4$  per simulation. The minimum and maximum number of families are 7 and 28 respectively and of the 500 configurations 102 exhibit 20 or more families of images. To  $z = 5.0$  there are 27 families in the Broadhurst et al. (2005) analysis. Although the mean number for our generated images is lower than that of the 27 strongly lensed sources in Abell 1689 by  $\sim 3\sigma$ , we do not consider this a serious problem. The total number of strongly lensed sources is within factor of 2 in 69 per cent of the 500 realizations.

We now examine the redshift distribution of the lensed sources in the simulations. The configurations are combined to produce a distribution of redshift probabilities in each bin. This allows the mean and standard deviation to be computed, see Fig. 2. Our simulated redshift distribution lies within  $1\sigma$  of the Abell 1689 sources, except for the  $0 \leq z < 1$  bin for which there are no observed multiply imaged sources in Abell 1689.

Finally we discuss the image properties themselves. Since the mass model does not include substructure, we do not expect to reproduce the source multiplicity distribution or the image magnitude distribution of Abell 1689 accurately. For a circular NFW mass profile, lensed sources with multiplicity of at most 3 can only be produced, whereas higher multiplicities are observed in Abell 1689. However, as shown in Fig. 2, the image magnitude distribution as generated through our source distribution does match that of Abell 1689, and the overall shape is reproduced.

Both 1) the total number, and the 2) redshift distribution of the simulated sources are consistent with the source characteristics of Abell 1689. Given the results of this comparison, we conclude that the HDF derived source population distribution is a faithful representation of the actual source distribution behind massive lensing clusters.

## 4.2 Cluster redshift distribution

In order to generate a set of massive, strong lensing clusters in our simulations, we need to derive redshifts from an observed cluster redshift distribution. To do so, we use the MAssive Cluster Survey (MACS) (Ebeling et al. 2001) sample as our template. We choose this sample since it is X-ray luminosity selected, which is a robust proxy for mass, and the *HST* follow-up of these clusters has demonstrated that a large majority of these are strong lenses (Ebeling 2005).

We use the binned MACS cluster redshifts (see fig. 9 in Ebeling et al. (2001)) to assign  $N_{\text{lens}}(z)$  to each redshift bin. The  $z = 0.000 - 0.025$  bin is omitted in the analysis since the cross-section for multiple imaging by clusters in this redshift range is negligible. An exponential fit is performed and the result is  $N_{\text{lens}}(z) = 136.07 \exp[-5.845 z]$ . The fit is then normalized, integrated and inverted to form a probability distribution. The final probability distribution returns a cluster lens redshift for use in the simulations in the range  $z = 0.025 - 0.600$  and can be expressed analytically as  $P_{\text{lens}}(x) = -0.171 \log_{10}[-0.83406(-1.0359 + x)]$ , where  $x$  is a random number between 0 and 1.

## 4.3 Cluster mass distribution

### 4.3.1 The NFW mass profile

The NFW density profile is derived from fits to cluster scale dark matter haloes that form in  $N$ -body simulations of a cold dark matter dominated Universe (Navarro, Frenk & White 1997). This density profile is given by,

$$\rho(r, z) = \frac{\rho_0}{((r^2 + z^2)^{1/2}/r_s)(1 + (r^2 + z^2)^{1/2}/r_s)^2} \quad (10)$$

where  $z$  is orientated along the line of sight and the radius  $r$  is orthogonal to the line of sight. There are two defining profile parameters for the NFW model, the characteristic density  $\rho_0$  and the scale radius of the profile  $r_s$ . The corresponding characteristic velocity dispersion  $v$  is defined as,

$$v^2 = \frac{4}{3} G r_s^2 \rho_0. \quad (11)$$

In our simulations we will calculate the total projected mass along the line of sight within the radius  $R = cr_s$ , where  $c$  is the concentration parameter. For  $R > r_s$  this is given by,

$$M(R) = \frac{3\pi v^2 r_s}{2G} \left[ \ln \left( \frac{R}{2r_s} \right) + \frac{1}{\sqrt{(R/r_s)^2 - 1}} \cos^{-1} \frac{r_s}{R} \right] \quad (12)$$

where  $R = cr_s$  (see Limousin, Kneib & Natarajan (2005) for further details on the profile).

### 4.3.2 Masses of the lensing clusters

Strong and weak lensing analysis of massive cluster lenses have determined that the total mass of such clusters within  $\sim 1$  Mpc, lies in the range,  $10^{14} - 10^{15} M_\odot$ , (Smith et al. 2005; Lombardi et al. 2005; Natarajan et al. 2007). This mass range is the starting point for our construction of simulated smooth cluster lenses.

Consider a cluster scale halo with an NFW profile. To generate the halo we first draw a total cluster mass from

the range  $10^{14} - 10^{15} M_\odot$  uniformly. We then assign profile parameters to characterize the mass distribution. A concentration is drawn randomly from the range  $c = 4 - 5$  (Bullock et al. 2001). Strong lensing models using NFW fitting profiles find that the typical scale radius lies in the range  $r_s = 200 - 400$  kpc. From the total mass,  $c$  and  $r_s$ , we compute the characteristic velocity dispersion of the NFW halo. Note that we ignore any scaling of  $\rho_0$  with cosmology for simplicity. Finally, with the halo structure determined, the ellipticity is then drawn randomly from  $0 \leq \epsilon \leq 0.15$ .

## 5 ANALYSIS OF THE SIMULATIONS

In this section we discuss the details of our simulations. Firstly, the procedure used to generate the lensing clusters and multiple image catalogues are discussed, and we explain how the source magnitude and redshift distribution and the cluster redshift distribution are used in the simulations. We then discuss our mass modeling assumptions. Finally, our marginalization method used to construct the confidence regions for cosmological parameter recovery are presented.

### 5.1 Cluster and lensed image generation

To perform our analysis, we generate clusters that will produce the requisite number of families of multiple images. The methods used to generate the cluster lenses are described in detail in Section 4.3.2. We choose all clusters that produce multiple images which can be detected via relative astrometry in the High Resolution Channel (HRC) of ACS. This means the effective Einstein radius  $R_E$ , which we compute at  $z = 6.0$ , must be less than  $50''$ . In addition to this upper bound we also apply a lower bound of  $R_E \geq 10''$ . This bound restricts the simulations to massive clusters that plausibly exhibit image configurations that are measurable with the HRC. We note there is no effect on the simulations if the maximum Einstein radius condition is dropped, as long as the same pixel resolution is maintained. This may be the case if observations were taken with the Wide Field Camera on *HST* and the images were processed with sub pixel dithering.

Once an appropriate cluster has been generated a source catalogue is generated. This catalogue is drawn from the HDF distribution derived in Section 4.1. A redshift and magnitude is assigned for each source using the distribution derived (numerically) from equation (9). Each source is also assigned a random position in the field of view  $4R_E \times 4R_E$ .

The number of sources in the catalogue for which magnitudes, redshifts and positions are generated, is dictated by the projected source number density of the ensemble HDF catalogue which is  $215 \text{ arcmin}^{-2}$  and the field of view. The source catalogue is then lensed with the code LENSTOOL (Kneib 1993; Jullo et al. 2007). The lensed catalogue is then sorted into single images and multiple image families.

At this point we have a complete simulated data set that is equivalent to a known observed sample of ideal lensing clusters. Observationally, this can be accomplished efficiently through high resolution space-based images of known massive clusters or deep ground based observations of clusters. We note that the MACS cluster survey provides a

catalogue of clusters selected through their X-ray luminosity. This cluster catalogue provides a useful starting point for observing programs to identify strongly lensing massive clusters. Such a systematic survey is currently underway (Ebeling 2005) on *HST* ACS.

## 5.2 Image catalogue construction

The image catalogues we use in our recovery of the cosmological parameters assume *HST* quality spatial resolution and spectroscopic redshifts. We first examine the ideal case, where the image positions and redshifts are known exactly. In Section 8 we expand our simulations to examine the effects of errors in the image positions and source redshifts. However, before considering possible sources of error, a best case scenario must be established when cluster lenses are stacked.

In the simulations, a magnitude limit is specified  $m_{\text{lim}}$ , when constructing the image catalogue from the lensed sources and is taken to be, unless otherwise stated,  $m_{\text{lim}} = 24.5$  in the AB(8140) band (Golse, Kneib, & Soucail 2002; Broadhurst et al. 2005). This ensures that all images will have measurable spectroscopic redshifts. Therefore, all families in the lensed image catalogue which do not have two images with magnitudes  $m < m_{\text{lim}}$  are removed at this point.

Applying the magnitude cut prior to the final selection of families in the image catalogue is a stringent requirement, since we only use images with  $m < m_{\text{lim}}$  in a given family. In the case of observational data, although it may not be possible to identify all members of a given image family spectroscopically, it is often possible to use properties like the image parity, morphology, photometric redshifts, or a combination of these to make the identification. Finally, since core images have been detected in lensing studies (Winn et al. 2004; Broadhurst et al. 2005), we do not remove such images unless they do not pass the magnitude cut.

## 5.3 Mass modelling

In the spirit of our simulations, where we are investigating the ideal case of stacking strong lensing clusters, we use the same form of the mass profile that was used to generate the image catalogue. The centre of the lens is fixed at the origin and the ellipticity and lens redshift are taken as known from the original cluster lens. In Section 7, we describe how the profile characteristics of the mass modelling influence the cosmology recovery. It is shown in Section 7 that for the NFW profile, the velocity dispersion and scale radius should be considered unknown in the cosmology recovery.

We note that the prior of a known mass profile is not the case when using observational data, where the underlying mass model is unknown. A variety of mass model priors will need to be considered in practise, since the mass distribution can be complicated, see for example the Bullet Cluster of Bradač et al. (2006). When observational data is analysed the cosmological parameter bias from the modelling of realistic clusters must be understood. These additional aspects present significant computational challenges when stacking a large number of clusters and we defer their study for the time being.

**Table 1.** Recovery Properties on the  $\Omega_{\text{M}}\text{-}w_{\text{X}}$  plane. The bounds are the limits of the  $1\sigma$  confidence contours, with the input cosmology  $(\Omega_{\text{M}}, w_{\text{X}}) = (0.27, -1.00)$  subtracted.  $A_1$  is the area enclosed by the  $1\sigma$  contour (see equation [14]).

Families	Clusters	$\Omega_{\text{M}}$ Bounds	$w_{\text{X}}$ Bounds	$A_1$
2	5	(-0.27,0.37)	(-1.00,0.15)	0.1825
	10	(-0.20,0.26)	(-0.56,0.11)	0.0855
	40	(-0.10,0.14)	(-0.21,0.08)	0.0227
	100	(-0.07,0.08)	(-0.10,0.05)	0.0061
3	5	(-0.26,0.21)	(-0.60,0.20)	0.1660
	10	(-0.14,0.14)	(-0.29,0.13)	0.0447
	40	(-0.09,0.08)	(-0.12,0.07)	0.0085
	100	(-0.05,0.05)	(-0.06,0.04)	0.0025
5	5	(-0.11,0.11)	(-0.17,0.08)	0.0149
	10	(-0.08,0.08)	(-0.12,0.08)	0.0094
	40	(-0.04,0.04)	(-0.06,0.04)	0.0023
	100	(-0.02,0.02)	(-0.02,0.02)	0.0004

## 5.4 Marginalization and cosmology recovery

The  $\chi^2$  minimization we use is computed in the source plane for computational speed, since the lens equation is many to 1 when mapping from the image plane to the source plane. Our measure is given by,

$$\chi^2 = \sum_{i=1}^f \sum_{j=1}^{n_i} \frac{\|\beta_{ij} - \langle\beta\rangle_i\|^2}{\langle\delta\beta^2\rangle_{ij}} \quad (13)$$

where  $\beta_{ij}$  is the source position corresponding to image  $j$  from the  $i^{\text{th}}$  family as mapped back through the lens equation (equation [1]), and  $\langle\delta\beta^2\rangle_{ij}$  is the standard deviation squared in the source plane. The mean source position,  $\langle\beta\rangle_i$ , is defined as  $\langle\beta\rangle_i = \sum_{j=1}^{n_i} \beta_{ij}/n_i$  and is the average over all source positions of images belonging to the  $i^{\text{th}}$  family. Therefore  $(\beta_{ij} - \langle\beta\rangle_i)$  is the difference between the observed image positions as viewed from the source plane.

In the calculation of equation (13),  $\langle\delta\beta^2\rangle_{ij}$  is computed using the assumed error in the image plane of  $\delta\theta = 0.1''$ . Using the known image position, we sample at eight image error points:  $(\theta_x, \theta_y \pm \delta\theta)$ ,  $(\theta_x \pm \delta\theta, \theta_y)$ ,  $(\theta_x \pm \delta\theta/\sqrt{2}, \theta_y \pm \delta\theta/\sqrt{2})$  and  $(\theta_x \mp \delta\theta/\sqrt{2}, \theta_y \pm \delta\theta/\sqrt{2})$ , and map each point back to the source plane using the lens equation. We then calculate the difference between  $\beta_{ij}$  and each of the mapped error points. The eight  $\delta\beta$  are first squared before averaging, i.e.  $\langle\delta\beta^2\rangle_{ij}$ , because this over estimates the standard deviation squared relative to the reverse order. Therefore using this averaging method leads to a *conservative estimate* of the final  $\chi^2$  and thus the confidence intervals (CIs).

The minimization routine, which uses a parabolic optimization in combination with parameter space bounds, is designed to ensure the  $\chi^2$  surface of each cluster is accurate to at least  $\delta\chi^2 \lesssim 0.002$ . This accuracy is sought because we want the final likelihood accurate to  $\lesssim 1$  per cent. After this is achieved we form the  $1\sigma$  to  $4\sigma$  CIs.

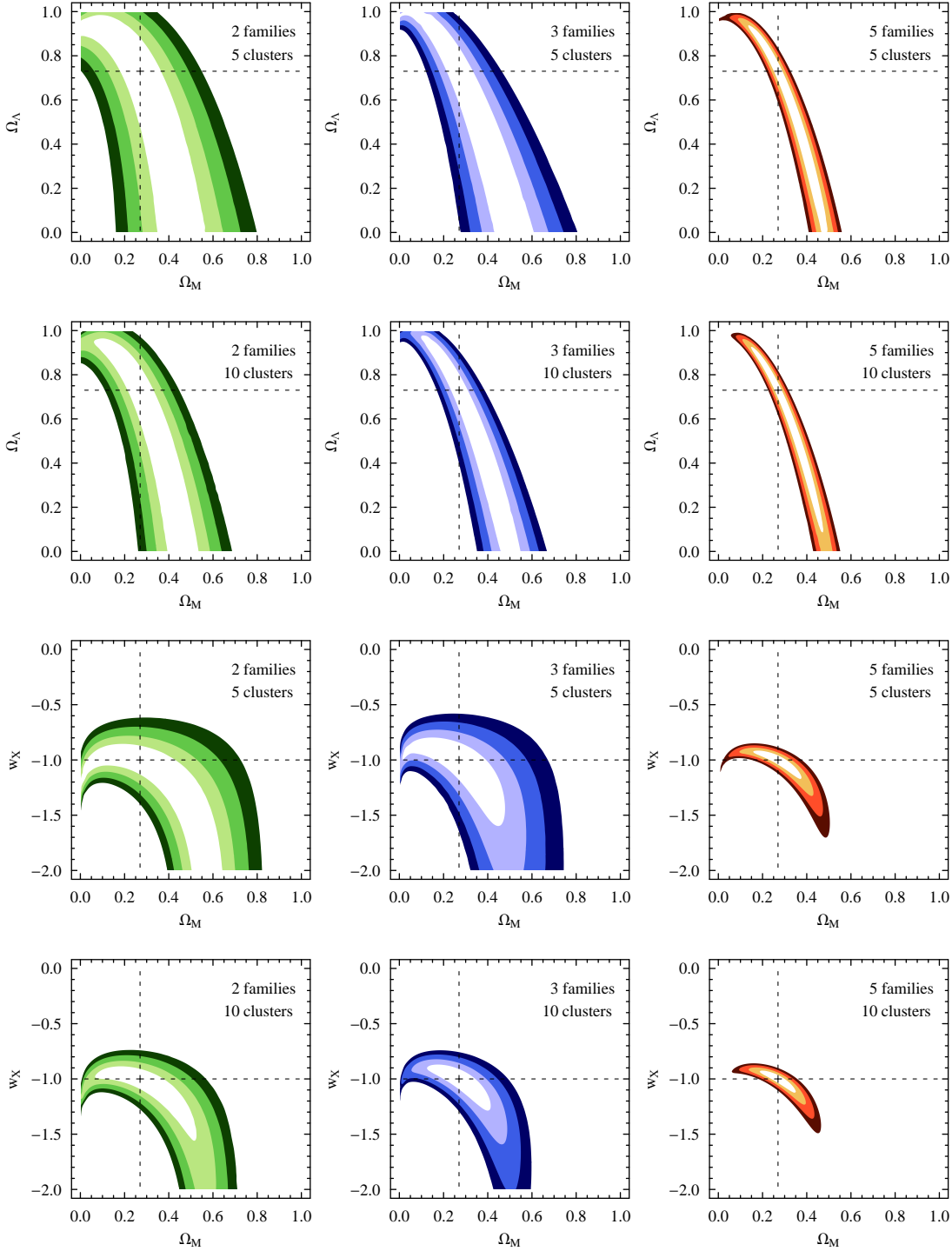


**Figure 3.** Confidence contours on the  $\Omega_M$ - $\Omega_\Lambda$  and  $\Omega_M$ - $w_X$  planes for 2, 3 and 5 multiple image families (columns 1, 2 and 3 respectively). For each family number specification, 5 or 10 clusters are stacked. The input cosmology marked by the cross in all panels, is a flat  $\Lambda$ CDM universe with  $(\Omega_M, \Omega_\Lambda, w_X) = (0.27, 0.73, -1.00)$ . In the top two rows  $w_X = -1.00$  and a flat universe is not assumed during the cosmology recovery. In the bottom two rows a flat cosmology is assumed with  $w_X$  and  $\Omega_M$  used in the cosmology recovery. In all panels, the recovery is undertaken with both the velocity dispersion and the scale radius allowed to vary. The  $1\sigma$  confidence region is the internal white region centred on the input cosmology. The  $2\sigma$ ,  $3\sigma$  and  $4\sigma$  confidence regions are progressively darker.



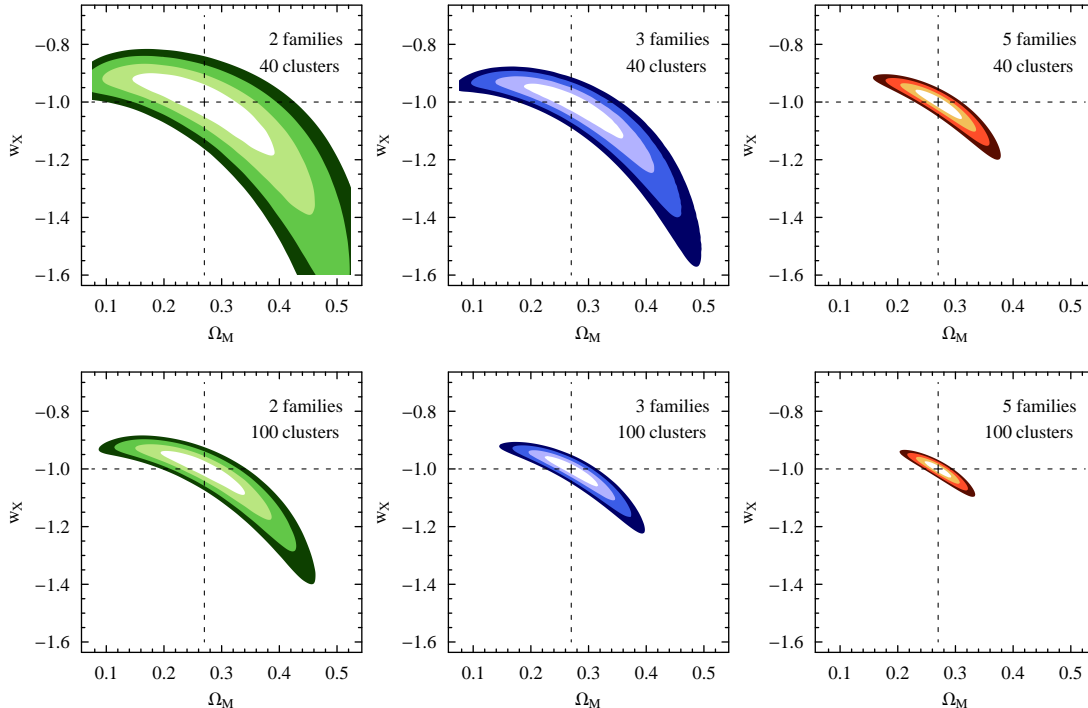


**Figure 4.** Cosmological constraints on the  $\Omega_M$ - $w_X$  plane for 40 and 100 stacked clusters (row 1 and 2 respectively) with 2, 3 and 5 multiple image families (columns 1, 2 and 3). A flat universe is assumed. Confidence region shading same as in Fig. 3.

## 6 RESULTS: RECOVERY OF INPUT COSMOLOGY

We investigate the cosmology recovery properties by considering cluster samples with different family numbers. To obtain the recovery properties, we proceed as outlined in Sections 4 and 5. At this stage the input parameters to the simulations are the number of clusters to stack, the total number of families in each cluster and the magnitude limits for the multiple images. The recovery properties are computed for each cluster, in the specified cosmological parameter space. The constraints from each cluster in the sample are then stacked to obtain the final recovery properties.

We consider observations of 5 and 10 clusters, with 2, 3 and 5 multiple image families. The magnitude limit,  $m_{\text{lim}}$ , is  $AB(8140) = 24.5, 24.5$  and  $26.0$  for the 2, 3 and 5 multiple image families respectively and the recovery properties of the input cosmology are computed in the  $\Omega_M$ - $\Omega_\Lambda$  and  $\Omega_M$ - $w_X$  planes. The results of stacking the first 5 generated clusters and then all 10 are shown in Fig. 3 and characterized in Table 1 for the  $\Omega_M$ - $w_X$  plane.

In the  $\Omega_M$ - $\Omega_\Lambda$  plane we observe that the parameter constraints obtained by *stacking* lensing clusters is insensitive to the value of the cosmological constant when marginalizing over  $\Omega_M$ . The  $\Omega_M$  constraints are also not stringent, with  $\Omega_M$  constrained to lie between approximately 0.1 and 0.50 for the 5 family 10 cluster case.

These properties of the cosmology recovery in the  $\Omega_M$ - $\Omega_\Lambda$  are expected. By examining Fig. 1, one can see that the contours passing through the input cosmology are degenerate for different source redshift configurations. This means

that the constraints derived from the family ratio will be tightest around the contour defined by the input cosmology.

However, in the  $\Omega_M$ - $w_X$  plane (lower two rows of Fig. 3) the family ratio is sensitive to the dark energy equation of state. In Fig. 1, we see that the  $\Xi$  contours passing through the input cosmology are quasi-orthogonal for different source redshift configurations. Therefore clusters with distinct source redshift planes will have different constraint directions in the  $\Omega_M$ - $w_X$  plane. This is also the case for different lens redshifts given the same two source redshifts however the effect less pronounced. When *stacking the cluster sample* the orthogonality of different family ratios leads to *closed* contours in the  $\Omega_M$ - $w_X$  plane, for the 5 family 10 cluster simulation.

We then examine the constraints obtained when 40 and 100 clusters are stacked for 2, 3 and 5 multiple image families. The magnitude limits are the same as for the 5 and 10 cluster runs but only the  $\Omega_M$ - $w_X$  plane is considered. The results are shown in Fig. 4 and Table 1. Note that 40 clusters with 5 families and 100 clusters with only 3 families, produce almost identical CIs.

## 7 DEPENDENCE ON LENS PARAMETERS

The role of the lens parameters in the optimal retrieval of the input dark energy equation of state is examined in this section. We address the issue of the  $\chi^2$  dependence on the marginalization over combinations of the dominant lens parameters. The marginalization for each parameter set is computed on the  $\Omega_M$ - $w_X$  plane in a flat Universe, for an input

cosmology  $(\Omega_M, w_X) = (0.27, -1.00)$ . We also consider the constraints derived from a full multi-dimensional marginalization and compare to the corresponding simple  $\chi^2$  minimization.

### 7.1 Marginalization over lens parameters

A massive NFW halo is considered in this section and substructure is omitted from the computations for the purpose of simplicity. The NFW halo is fixed at the origin and the parametrization we use is typical of massive cluster lenses (Natarajan et al. 2007) and the lens parameters we use are:  $v = 1600 \text{ km s}^{-1}$ ,  $r_s = 200 \text{ kpc}$  and  $\epsilon = 0.10$ , with the lens redshift  $z_1 = 0.3$ . Two sources are lensed and they are located at  $(x_1, y_1) = (-1.00, 0.10)$  and  $(x_2, y_2) = (1.20, 4.80)$  respectively, with redshifts  $z_{s1} = 1.0$  and  $z_{s2} = 3.0$ . Sources 1 and 2 have multiplicities of 5 and 3 respectively.

#### 7.1.1 Case with known lens parameters

First we consider the case where one has complete knowledge of the gravitational lens, i.e. all lens parameters are known exactly. The result of the marginalization with all lens parameters fixed is shown in the upper left panel of Fig. 5 for the NFW lensing cluster. Note that the confidence region for the NFW profile is non-zero. In fact, the existence of a non-zero confidence region is a general feature of the lensing systems in our simulations.

Based on Fig. 5 it is clear that the intrinsic confidence region of a lensing system represents a fundamental limit on the determination of the cosmological parameters from a single configuration. Even in the optimal scenario, i.e. complete knowledge of the lens system, one must consider the confidence region and not the best fitting cosmology in a rigorous statistical treatment. The best-fitting cosmological parameters, as for example employed in Dalal, Hennawi & Bode (2005), cannot be used to characterize the cosmological parameter recovery, since they do not take into account the limitation of the intrinsic confidence region. Noting this property, we have used CIs exclusively in this work.

#### 7.1.2 Mass profile parameters

In practice, one does not have prior information on all the parameters defining the mass profile of an observed lensing cluster. For the NFW lensing profile, there are three combinations of the lens parameters to consider marginalizing over when recovering the cosmology. These are: the velocity dispersion  $v$ , the scale radius  $r_s$  and both  $v$  and  $r_s$ . The results of each marginalization are given in Fig. 5.

For the NFW profile, the shape of the confidence contours changes for the different marginalization parameters. For the case of marginalization over  $r_s$  alone, in which  $v$  is held fixed, closed confidence contours are obtained in the  $\Omega_M$ - $w_X$  plane. This is distinct from the contours derived for the marginalization over  $v$  alone, which yields a confidence region which follows the contours of constant cosmological family ratio  $\Xi$ . In Fig. 5, the simultaneous marginalization of  $r_s$  and  $v$  expands the  $4\sigma$  confidence region asymmetrically. In addition, note that all other confidence contours qualitatively follow the contours for the family ratio. Therefore it is

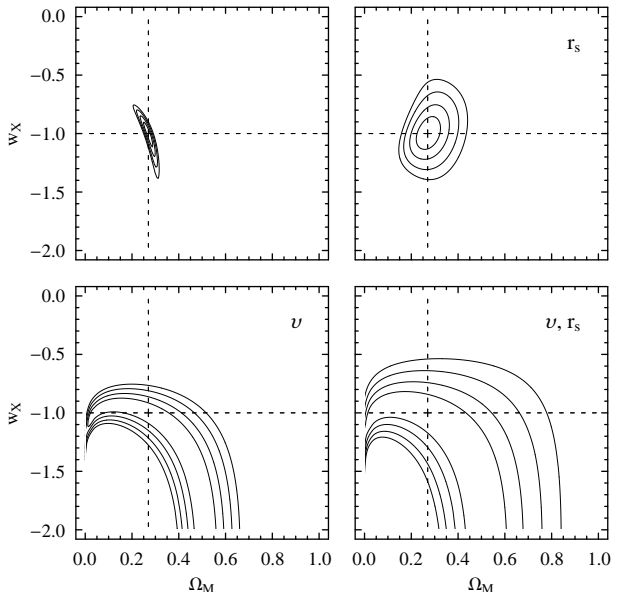


**Figure 5.** Marginalization contours over different NFW parameters. The  $1\sigma$  to  $4\sigma$  contours in the  $\Omega_M$ - $w_X$  plane are shown, and the cross marks the input cosmology  $(\Omega_M, w_X) = (0.27, -1.00)$ . The parameter(s) in the upper right corner of each panel specify the marginalization variable(s).

obvious that optimization over both the characteristic density and scale radius is required when recovering cosmology constraints from the NFW profile.

An additional comment on Fig. 5 is warranted with regard to the cosmology recovery. It is obvious from the panels in Fig. 5 that when only  $r_s$  or only  $v$  are allowed to vary, that tighter cosmological constraints are obtained, compared to the case where both  $r_s$  and  $v$  are marginalized over simultaneously (bottom right panel of Fig. 5). It is therefore natural to ask, what are the cosmology recovery properties in the cases where only  $r_s$  or  $v$  are marginalized for stacked clusters? However, when considering actual cluster lenses, if we were to marginalize over say only  $r_s$ , we would have to fix the velocity dispersion. This would require an additional prior, and in actual cluster lenses this prior is not typically available. It may be possible to constrain the total cluster mass through X-ray observations, and in this case, one would use equation (12) to apply the priors to *both* the velocity dispersion and the scale radius. However, in general, when using an NFW profile to model an actual strong lensing cluster, both  $r_s$  and  $v$  are not known a priori (Comerford et al. 2006). The reader should therefore note that although stronger cosmological constraints could be obtained if  $r_s$  or  $v$  were known a priori, this is not the case in actual cluster models because separate priors on  $r_s$  or  $v$  cannot be found. To this end, we have only presented the marginalization over both  $r_s$  and  $v$  in Section 6.

### 7.2 Full marginalization versus $\chi^2$ minimization

Up to this point, we have considered a simple minimization routine of the lens parameters with respect to the  $\chi^2$  estimator. We have done this over the cosmological plane and for

different lens parameter combinations for the NFW profile. However, we now examine the validity of this assumption for the NFW lensing configuration in Section 7.1.

We now perform a full multi-dimensional marginalization over the lens parameters,  $r_s$  and  $v$ , for the NFW lensing configuration. Our adopted method is as follows: first, we find the optimized lens parameters which gives the minimum  $\chi^2_{\min}$  at each cosmology point. From the optimized lens parameters, we then compute a  $\chi^2$  surface extending to  $\chi^2 = (\chi^2_{\min} + 50)$ . The parameter spacing on the  $\chi^2$  surface is 0.2 arcsec for  $r_s$  and 0.2 km s<sup>-1</sup> for  $v$ . The  $\chi^2$  surface is then converted into a likelihood surface using,  $\mathcal{L} = \exp(-\chi^2/2)$ , which is integrated to obtain the marginalized likelihood at a given cosmology input. This likelihood is then converted to a  $\chi^2$  surface, using  $\chi^2 = -2\ln(\mathcal{L}/\mathcal{L}_{\max})$ .

To quantify the difference between the multi-dimensional marginalization and the simple optimization method, we consider an integral which characterizes the enclosed area,

$$A_n = \int_{R(n)} d\Omega_M d\omega_X \quad (14)$$

where  $n$  defines the confidence contour, and  $R(n)$  the region enclosed by the given contour.

For the multi-dimensional marginalization over  $r_s$  and  $v$ , we have approximately,  $A_1 = 0.267$ ,  $A_2 = 0.462$ ,  $A_3 = 0.680$  and  $A_4 = 0.889$ . Whereas for the simple  $\chi^2$  minimization  $A_1 = 0.273$ ,  $A_2 = 0.464$ ,  $A_3 = 0.683$  and  $A_4 = 0.890$ . The difference between the enclosed area is largest for  $A_1$ , which is  $\sim 2$  per cent. Importantly, the  $1\sigma$  contour from the simple optimization method encloses an area larger than the full multi-dimensional marginalization. Both methods recover a  $\chi^2 = 0$  at the input cosmology.

Given the maximum  $\sim 2$  per cent difference between the enclosed areas from the multi-dimensional marginalization and the simple  $\chi^2$ -optimization, we are justified in using the simple optimization method. With sufficient multiple images to constrain the cluster potential, one expects only one global minimum in the  $\chi^2$  optimization surface. This is the case for the NFW lensing configuration considered here, and for similar lensing configurations one expects the optimization method to accurately reproduce the confidence contours derived from a full multi-dimensional marginalization.

## 8 STUDY OF SURVEY CHARACTERISTICS

We have also simulated smooth cluster lenses that contain observational noise. The noise sources we have considered are positional errors and redshift error. These two sources are the two major observational parameters which will determine the type of survey required for the application of CSL. Our simulations are restricted to the 5 families 10 cluster case (see bottom right panel in Fig. 3) in the  $\Omega_M$ - $\omega_X$  plane.

Our objective is to examine the levels of noise which do not lead to relaxation of the CIs, when compared to our simulations of the ideal case. We use this approach since this will represent a tolerance threshold where parameter constraints will weaken.

First we consider redshift accuracy. We have re-run the 5 families 10 cluster simulation with gaussian red-

shift noise with the following standard deviations  $\Delta z = 0.003, 0.005, 0.01$ , and 0.1. When adding the noise to the source redshift, we draw from the appropriate gaussian and add the resultant value to the known redshift. Note that all multiple images of a given family receive the same noise contribution to their redshift. Our results are as follows. We find that photometric redshift accuracy, i.e.  $\Delta z = 0.1$ , leads to significant relaxing of the CIs and in some cases does not recover the input cosmology correctly. Of the remaining standard deviation simulations, all recover the input cosmology with increasingly tighter constraints. For  $\Delta z = 0.003$ , there is negligible confidence contour relaxation when compared to the ideal simulation.

Next we move onto image positions. Following a similar procedure to the redshifts, we find that a positional accuracy of  $\pm 2$  pixels of the *HST* ACS is required to recover the confidence region in the  $\Omega_M$ - $\omega_X$  plane. This means that space based imaging of the strong lensing clusters will be required. We have also considered image position error in combination with redshift error, and find that the combination  $\Delta z = 0.003$  and  $\pm 2$  pixels in ACS does not lead to relaxation of the confidence contours compared to the ideal case. This means that space based imaging of strong cluster lenses, followed up by spectroscopic redshift determination of the multiple images, is the appropriate survey method to pursue for the application of CSL to cosmography.

## 9 LIMITATIONS OF OUR CURRENT ANALYSIS

As with any other method used to constrain cosmological parameters, CSL has a number of sources of error one must consider. Our goal has been to examine observational strategies under the most optimal conditions in this first detailed study. Our results demonstrate that by stacking lensing clusters with several multiple image families, confidence regions for the input cosmological parameters can be recovered, as shown in Figs 3 and 4.

In earlier work, Dalal, Hennawi & Bode (2005) raised the issue of parameter bias introduced by the unknown cluster mass profile, and the presence of substructure. They concluded from extracting the best-fitting cosmological parameters (rather than confidence regions) that this technique produces  $> 100$  per cent errors for a single cluster. We are not disputing the importance of correctly modelling the mass profile and substructure. However, in our simulations we have focused on the recovery properties of the ideal scenario, and the errors cosmography CSL can tolerate in an observational data set.

Dalal, Hennawi & Bode (2005) has also investigated the recovery bias including line of sight density fluctuations using a single numerical cluster. It should also be pointed out that any parameter recovery bias resulting from substructure along the line of sight (fig. 4 of Dalal, Hennawi & Bode (2005)), will be minimized if uncorrelated lines of sight are used when constructing the cosmological constraints. Also, bias due to line of sight substructure could possibly be accounted for, by performing redshift surveys behind cluster lenses and modeling any detected structure along the line of sight in multiple lens planes. Removing the systematic parameter bias due to substructure along the line of sight is

an important topic that requires further investigation and is left for future work.

Since we have only used positional accuracy in our cosmological recovery, we should ask: What additional  $\chi^2$  measures can we add to our current recovery measure of equation (13) that will further constrain the input cosmology? The first obvious candidate is a higher order shape estimators for multiple images, since we have ignored all shapes and simply used a point approximation in our simulations. In real clusters multiply imaged sources will have their shapes distorted as they are strongly lensed and this will give additional information about the lensing mass distribution, see for example Leonard et al. (2007). Another improvement may come from the possibility of using other observational maps of clusters to infer additional properties of the cluster. For example, a total mass constraint can be obtained from X-ray cluster observations.

## 10 CONCLUSIONS

In this paper, we have examined the recovery of input cosmological parameters using the cosmological family ratio for several sets of multiple images in stacked simulated smooth lensing clusters. For a given lensing configuration, the constraints on the  $\Omega_M$ - $w_X$  plane are tighter than those on the  $\Omega_M$ - $\Omega_\Lambda$  plane. We find that the recovery of input parameters depends both on the number of multiple image families with known redshifts and the number of clusters stacked.

As shown in Figs 3 and 4, the confidence contours tighten as we increase the number of families from 2 - 5, and as the total number of stacked clusters is increased from 1 - 100. For example, the recovery is comparable in terms of area enclosed within the  $1\sigma$  -  $4\sigma$  contours for the case with 5 families using 40 clusters and 3 families using 100 clusters. As we demonstrate, both strategies – stacking fewer clusters with a larger number of image families or a larger number of clusters with fewer families lead to comparable constraints.

Currently there are about 40 clusters with high resolution *HST* ACS images, of which a handful (about 7 - 10) have more than 3 families of multiple images with measured redshifts. Proposed future space missions, the James Webb Space Telescope and JDEM will enlarge the existing lensing cluster samples by a factor of 20 or more, while simultaneously detecting a larger number of families on average for each cluster through very deep imaging. Determining spectroscopic redshifts for multiple image families is likely the limiting step in terms of the observational effort for the CSL method.

If 10 clusters with 3 multiply imaged sources are stacked, the dark energy equation of state in a flat universe can be constrained to  $-1.6 \lesssim w_X \lesssim -0.8$  at  $2\sigma$  where  $\Omega_M$  has been marginalized over, see Fig. 3. This is comparable with current methods (Komatsu et al. 2009). Therefore to be competitive with current methods, given that actual massive cluster lenses will present sub-optimal recovery conditions relative to those considered here, an initial application of CSL to actual lensing clusters will require at least 10 clusters with 3 or more multiply imaged sources with Abell 1689 quality *HST* ACS images. Such constraints may be obtained only if the source redshifts are determined spectroscopically. These factors indicates that initial observations should focus

on massive clusters that exhibit large lensing cross sections. Once these strong lensing clusters are imagined to Abell 1689 quality with the *HST*, those with 3 or more multiply imaged sources should be given priority when determining which lensing clusters to follow up spectroscopically.

## ACKNOWLEDGMENTS

We acknowledge useful discussions with Jean-Paul Kneib.

## REFERENCES

- Allen S. W., Schmidt R. W., Ebeling H., Fabian A. C., van Speybroeck L., 2004, *MNRAS*, 353, 457
- Bacon D. J., Refregier A. R., Ellis R. S., 2000, *MNRAS*, 318, 625
- Biesiada M., 2006, *Phys. Rev. D*, 73, 023006
- Blandford R. D., Narayan R., 1992, *ARA&A*, 30, 311
- Bradač M. et al., 2006, *ApJ*, 652, 937
- Broadhurst T. et al., 2005, *ApJ*, 621, 53
- Bullock J. S., Kolatt T. S., Sigad Y., Somerville R. S., Kravtsov A. V., Klypin A. A., Primack J. R., Dekel A., 2001, *MNRAS*, 321, 559
- Casertano S. et al., 2000, *AJ*, 120, 2747
- Comerford J. M., Meneghetti M., Bartelmann M., Schirmer M., 2006, *ApJ*, 642, 39
- Cooray A. R., 1999, *ApJ*, 524, 504
- Dalal N., Hennawi J. F., Bode P., 2005, *ApJ*, 622, 99
- Ebeling H., Edge A. C., Henry J. P., 2001, *ApJ*, 553, 668
- Ebeling H., 2005, *HST prop.* 10491
- Efstathiou G. et al., 2002, *MNRAS*, 330, L29
- Fernández-Soto A., Lanzetta K. M., Yahil A., 1999, *ApJ*, 513, 34
- Gabasch A., Goranova Y., Hopp U., Noll S., Pannella M., 2008, *MNRAS*, 383, 1319
- Gavazzi R., Treu T., Koopmans L. V. E., Bolton A. S., Moustakas L. A., Burles S., Marshall P. J., 2008, *ApJ*, 677, 1046
- Golse G., Kneib J.-P., Soucail G., 2002, *A&A*, 387, 788
- Hinshaw G. et al., 2009, *ApJS*, in press (arXiv:0803.0732)
- Jullo E., Kneib J.-P., Limousin M., Elíasdóttir Á., Marshall P. J., Verdugo T., 2007, *NJPh*, 9, 447
- Kaiser N., 2000, *ApJ*, 537, 555
- Kneib J.-P., 1993, PhD thesis, Université Paul-Sabatier, Toulouse
- Komatsu E. et al., 2009, *ApJS*, in press (arXiv:0803.0547)
- Leonard A., Goldberg D. M., Haaga J. L., Massey R., 2007, *ApJ*, 666, 51
- Link R., Pierce M. J., 1998, *ApJ*, 502, 63
- Limousin M., Kneib J.-P., Natarajan P., 2005, *MNRAS*, 356, 309
- Limousin M. et al., 2007, *ApJ*, 668, 643
- Lombardi M. et al., 2005, *ApJ*, 623, 42
- Macciò A. V., 2005, *MNRAS*, 361, 1250
- Meneghetti M., Bartelmann M., Dolag K., Moscardini L., Perrotta F., Baccigalupi C., Tormen G., 2005, *A&A*, 442, 413
- Meneghetti M., Jain B., Bartelmann M., Dolag K., 2005, *MNRAS*, 362, 1301

- Natarajan P., De Lucia G., Springel V., 2007, *MNRAS*, 376, 180
- Navarro J. F., Frenk C. S., White S. D. M., 1997, *ApJ*, 490, 493
- Paczynski B., Gorski K., 1981, *ApJ*, 248, L101
- Perlmutter S. et al., 1999, *ApJ*, 517, 565
- Riess A. G. et al., 1998, *AJ*, 116, 1009
- Riess A. G. et al., 2004, *ApJ*, 607, 665
- Riess A. G. et al., 2007, *ApJ*, 659, 98
- Sahni V., Starobinsky A., 2006, *IJMPD*, 15, 2105
- Seljak U. et al., 2005, *Phys. Rev. D*, 71, 103515
- Semboloni E. et al., 2006, *A&A*, 452, 51
- Sereno M., 2002, *A&A*, 393, 757
- Smith G. P., Kneib J.-P., Smail I., Mazzotta P., Ebeling H., Czoske O., 2005, *MNRAS*, 359, 417
- Soucail G., Kneib J.-P., Golse G., 2004, *A&A*, 417, L33
- Spergel D. N. et al., 2003, *ApJS*, 148, 175
- Spergel D. N. et al., 2007, *ApJS*, 170, 337
- Tonry J. L. et al., 2003, *ApJ*, 594, 1
- van Waerbeke L. et al., 2000, *A&A*, 358, 30
- Villumsen J. V., Freudling W., da Costa L. N., 1997, *ApJ*, 481, 578
- Wambsganss J., Bode P., Ostriker J. P., 2005, *ApJ*, 635, L1
- Winn J. N., Rusin D., Kochanek C. S., 2004, *Nature*, 427, 613
- Williams R. E. et al., 1996, *AJ*, 112, 1335
- Wittman D. M., Tyson J. A., Kirkman D., Dell'Antonio I., Bernstein G., 2000, *Nature*, 405, 143
- Yahata N., Lanzetta K. M., Chen H.-W., Fernández-Soto A., Pascarella S. M., Yahil A., Puetter R. C., 2000, *ApJ*, 538, 493

This paper has been typeset from a  $\text{\TeX}/\text{\LaTeX}$  file prepared by the author.